

No More Ambiguity in 360° Room Layout via Bi-Layout Estimation

Yu-Ju Tsai^{1,3*} Jin-Cheng Jhang^{2*} Jingjing Zheng³ Wei Wang³
 Albert Y. C. Chen³ Min Sun^{2,3} Cheng-Hao Kuo³ Ming-Hsuan Yang¹
¹UC Merced ²National Tsing Hua University ³Amazon
 {ytsai17, myang37}@ucmerced.edu {frank890725}@gapp.nthu.edu.tw
 {zhejingj, wweiwan, aycchen, minnsun, chkuo}@amazon.com

Abstract

Inherent ambiguity in layout annotations poses significant challenges to developing accurate 360° room layout estimation models. To address this issue, we propose a novel Bi-Layout model capable of predicting two distinct layout types. One stops at ambiguous regions, while the other extends to encompass all visible areas. Our model employs two global context embeddings, where each embedding is designed to capture specific contextual information for each layout type. With our novel feature guidance module, the image feature retrieves relevant context from these embeddings, generating layout-aware features for precise bi-layout predictions. A unique property of our Bi-Layout model is its ability to inherently detect ambiguous regions by comparing the two predictions. To circumvent the need for manual correction of ambiguous annotations during testing, we also introduce a new metric for disambiguating ground truth layouts. Our method demonstrates superior performance on benchmark datasets, notably outperforming leading approaches. Specifically, on the MatterportLayout dataset, it improves 3D IoU from 81.70% to 82.57% across the full test set and notably from 54.80% to 59.97% in subsets with significant ambiguity.

1. Introduction

Room layout estimation from a single 360° image has received significant attention due to the availability of cheap 360° cameras and the demonstration of visually pleasing room pop-ups. It also plays a vital role in indoor 3D scene understanding [3, 15, 32, 38] as the room layout constrains the space where objects are placed and interact. Its performance has improved significantly over the years, where the gain comes from better algorithms design [17, 29, 31, 34], and more challenging data collected [7, 45]. Despite the progress, the task formulation of predicting a *single* layout

*Equal contribution

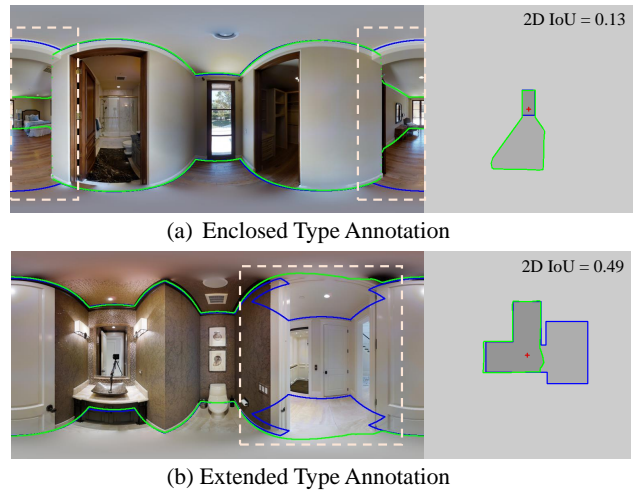


Figure 1. **Inherent ambiguity in the MatterportLayout [45].** Blue and Green represent ground truth annotations and predictions from the SoTA models, respectively. The layout boundaries are shown on the left, and their bird’s-eye view projections are on the right. We define two types of layout annotation: (a) **enclosed type** encloses the room. (b) **extended type** extends to all visible areas. The dashed lines underscore the ambiguity in the dataset labels.

given a *single* 360° image has never been changed.

Annotating a *single* layout for each 360° image is, in fact, an ambiguous task. For instance, consider the two images with openings in Fig. 1, where the ground truth (GT) annotation stops at openings and encloses the nearest room in Fig. 1(a) while extending to all visible areas inside the opening in Fig. 1(b). Notably, even within the same dataset, there are variations in how opening regions are annotated. We observe that this ambiguity issue in annotation is prevalent across most datasets, and there is a lack of a clear definition of how to annotate ambiguous regions. Furthermore, state-of-the-art (SoTA) methods often overlook this ambiguity issue, leading to inherent inaccuracy during training. As a result, existing methods may predict in a manner opposite to the GT, as shown in Fig. 1. In this paper, we define two main types of layout annotations: *enclosed* and *extended*. The former

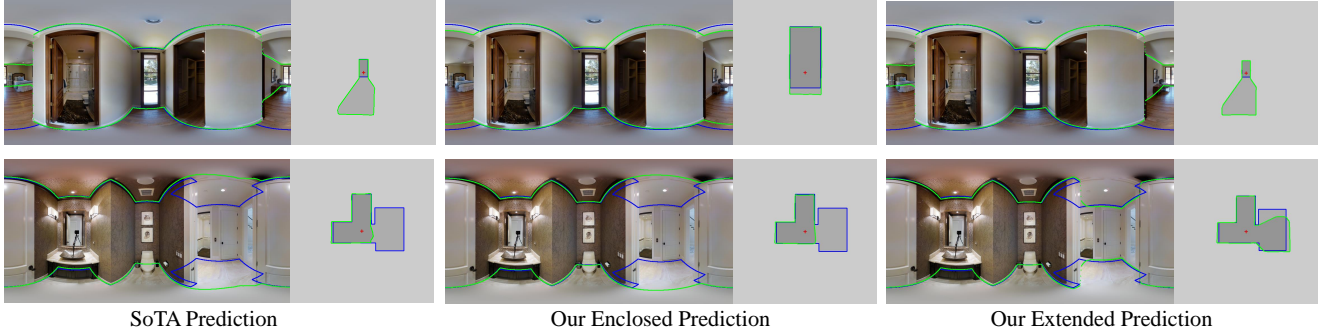


Figure 2. **Comparisons of our Bi-Layout model and the SoTA models.** Blue and Green indicate ground truth labels and predictions, respectively. For each image, the layout boundaries are shown on the left, while their bird’s-eye view projections are shown on the right. Our Bi-Layout model can predict two extremely different types of layouts (*enclosed* and *extended*), addressing the ambiguity issue that the SoTA methods struggle with.

stops at ambiguous regions and encloses the room, whereas the latter extends to all visible areas inside the opening.

To address the confusion arising from the ambiguity issue in model training, as shown in Fig. 3, we propose a novel Bi-Layout model to simultaneously predict both *enclosed* and *extended* layouts for each image. Our model consists of three components: a shared feature extractor, two separate global context embeddings, and a shared feature guidance module. Two separate global context embeddings are learned to encode all context information related to the corresponding layout type. The shared feature guidance module guides the fusion of the shared image feature with our two embeddings separately through cross-attention. Specifically, we use the image feature as the query and each global context embedding as the key and value. When queried by the image feature, the global context embedding can inject layout type-related context information into the image feature. This results in enhanced alignment of the image feature with the corresponding layout prediction type.

Our model design introduces two key innovations. First, contrary to the standard Query-Key-Value setting employed in DETR [2] and other high-level tasks [4, 5, 20, 30, 37, 42], where embeddings serve as queries to retrieve relevant information from the image feature, we invert this relationship and employ our image feature as the queries. This unconventional design allows the image feature to be guided by our embedding, which represents the global information of a specific layout type. To the best of our knowledge, we are the first to develop a query-based model for room layout estimation, inherently designed for predicting multiple layouts. The second innovation lies in the efficiency of our model, which can predict two layouts with minimal additional model size overhead. For bi-layout estimations, naive approaches either train two distinct models with identical architectures on different labels or train a single model by sharing the feature extractor but separating other components. However, the former method doubles the model size and training time, while the latter lacks compactness and grapples with interference

in simultaneously learning two layout types. In contrast, our model is not only the smallest, achieved by sharing both the feature extractor and the guidance module, but it also avoids interference issues by employing separate global context embeddings to guide feature fusion for different layout types. As shown in Fig. 2, our model is able to predict two extremely different layouts.

We also introduce a new metric termed as *disambiguate* metric to resolve ambiguities in the annotations of test data. It calculates the Intersection over Unions (IoU) of both predicted layouts with the ground truth and selects the higher IoU for evaluation. This is an effective way to quantitatively measure the benefit of our Bi-Layout estimation without manually correcting ambiguous annotations during testing. Another noteworthy feature of our Bi-Layout model is its ability to detect ambiguous regions with reasonable precision and recall by comparing two predictions. Our method exhibits superior performance on benchmark datasets, surpassing SoTA methods. On MatterportLayout [45], it enhances 3DIoU from 81.70% to 82.57% on the entire test set and notably from 54.80% to 59.97% in subsets with substantial ambiguity.

The main contributions of this work are:

- We clearly identify layout ambiguity issues in existing datasets and propose a *disambiguate* metric to measure the accuracy with multiple predictions effectively.
- We propose a novel Bi-Layout model that utilizes two global context embeddings with a shared feature guidance module to generate multiple layout predictions while keeping the model compact.
- We evaluate our method with extensive experiments and prove it outperforms SoTA methods in all settings, showing that our Bi-Layout model effectively resolves the layout ambiguity issues.

2. Related Work

360° room layout estimation. In 360° room layout estimation, prior methods follow the Manhattan World as-

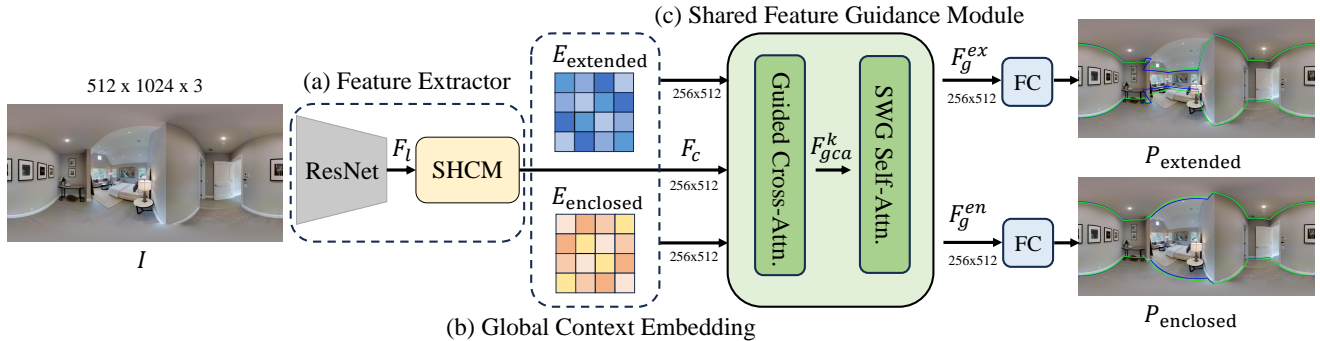


Figure 3. **Our Bi-Layout network architecture.** (a) **Feature extractor:** It processes a panoramic image I using ResNet-50 to extract multi-scale features F_l and then feeds those features into the Simplified Height Compression Module (SHCM) to produce the final compressed feature F_c . (b) **Global Context Embedding:** It consists of two learnable embeddings E_k , each designed to capture and encode the contextual information inherent in the corresponding type of layout labels. (c) **Shared Feature Guidance Module:** It consists of two components: Guided Cross-Attention and SWG Self-Attention. It guides the fusion of compressed feature F_c with the global context embedding E_k to generate feature F_g^k ($k \in [extended, enclosed]$) more aligned for the corresponding layout type. Finally, we use fully connected (FC) layers to map F_g^k to horizon-depth and room height, which are further converted to boundary layouts ($P_{extended}$ and $P_{enclosed}$).

sumption [6]. For instance, LayoutNet [44] predicts corner and boundary probability maps directly from panoramas. Dula-Net [36] predicts 2D-floor plane semantic masks from equirectangular and perspective views of ceilings. Zou *et al.* presents improved versions, LayoutNet v2, and Dula-Net v2 [45], demonstrating enhanced performance on cuboid datasets. Fernandez *et al.* adopts equirectangular convolutions (EquiConvs) [8] for generating corner and edge probability maps. HorizonNet [31] and HoHoNet [32] simplify layout estimation by employing 1D representations and employing Bi-LSTM [14, 27] and multi-head self-attention mechanisms [33] to establish long-range dependencies. LED²-Net [34] reformulates layout estimation as predicting the depth of walls in the horizontal direction. AtlantaNet [24] predicts room layouts by combining projections of the floor and ceiling planes. DMH-Net [41] transforms panorama into cubemap [9] and predicts the position of intersection lines with learnable Hough Transform Block [40]. LGT-Net [17] employs self-attention transformers [33] to learn geometric relationships and capture long-range dependencies. DOP-Net [29] disentangles 1D feature by segmenting features into orthogonal plane representation, and uses GCN [18] and transformer [33] to refine the features.

These methods are designed only to predict a single layout, which often encounters challenges posed by the inherent ambiguity in dataset labels, resulting in suboptimal performance. In contrast, our Bi-Layout model addresses this issue by generating two distinct layout predictions through the innovative integration of global context embeddings and our shared feature guidance module design.

Multiple layout hypotheses. Several prior studies [10, 12, 13, 19, 25, 26, 28, 35, 39] have employed multiple hypotheses in their methods for estimating room layouts. The fundamental concept behind these methods involves leveraging vanishing points, edges, or other pertinent information to

generate several rays or boxes as potential layout hypotheses. Through various scoring function designs, one of the hypotheses can be selected as the prediction that best fits the room. In contrast, our method generates two distinct layout predictions, which can also be viewed as having two hypotheses. However, the key disparity lies in the fact that the previous methods only have one hypothesis defining the correct geometry. On the contrary, both of our predictions are meaningful and offer two different geometries, *extended* and *enclosed* layouts, allowing for flexibility in choosing the suitable one based on the specific requirements of different use cases.

Query-based vision transformer. Transformers [33] have exhibited considerable efficacy in various high-level computer vision tasks, including object detection [2, 43], segmentation [4, 5], tracking [20, 42], and floorplan reconstruction [30, 37]. The standard transformer decoder utilizes feature embeddings as queries to extract relevant features from the image feature, which acts as both the key and value. Unlike the standard query-based transformer, our proposed design utilizes the image feature as the query with our global context embedding as the key and value. This unique design allows our model to predict two distinct layouts, a departure from prior methods that predict only a single layout.

3. Inherent Ambiguity in Labeled Data

We systematically examine instances of low IoU in the SoTA methods [17, 29, 34] using MatterportLayout dataset [45]. Our analysis identifies two types of ambiguity. First, when an *enclosed* type GT label is given, the SoTA methods predict regions located outside of that designated room (See Fig. 1(a)). Conversely, when an *extended* type GT label is given, the SoTA methods concentrate on the room where the camera is positioned (See Fig. 1(b)). These findings underscore inherent ambiguity within the testing GT labels. Moreover, since

the SoTA models will predict either *enclosed* or *extended* types of layouts, the same ambiguity is likely to be within the training GT labels as well. This presents a substantial challenge for single-prediction-based SoTA methods.

4. Method

To address the ambiguity issue in the dataset labels, we introduce our Bi-Layout model as shown in Fig. 3, which can generate two types of layout predictions P_{extended} and P_{enclosed} . Our model mainly consists of three modules: feature extractor (Sec. 4.1), global context embedding (Sec. 4.2), and shared feature guidance module (Sec. 4.3). We describe each component and the training objectives (Sec. 4.4) used for training our Bi-Layout model in the following sections.

4.1. Feature Extractor

The feature extractor in our Bi-Layout model is shown in Fig. 3(a). We follow previous works [17, 29, 31, 34] to use ResNet-50 [11] architecture to extract 2D image features F_l of 4 different scales from the input panorama I . For each feature scale, we modify the module from [31] as *Simplified Height Compression Module* (SHCM) to compress the features along the image height direction and generate 1D feature of the same dimension $\mathbb{R}^{N \times \frac{D}{4}}$, where N is the width of feature map and D is the feature dimension. Finally, we concatenate these features from different scales to generate the final compressed feature $F_c \in \mathbb{R}^{N \times D}$, where $N = 256$ and $D = 512$.

In contrast to previous works [17, 31, 34] setting $D = 1024$, our design reduces model parameters. By pruning our feature representation, we enhance the model’s efficiency without compromising its effectiveness. To assess this design choice, we present detailed ablation studies in Sec. 5.5.

4.2. Global Context Embedding

Once the compressed feature F_c is extracted, we introduce a novel and learnable embedding mechanism termed as *Global Context Embedding*. This mechanism captures and encodes the overarching contextual information in a specific layout label, as illustrated in Fig. 3(b). We employ two learnable embeddings $E_k \in \mathbb{R}^{N \times D}$ where $k \in [\textit{extended}, \textit{enclosed}]$, one for *extended* and the other one for *enclosed* type. During training, these embeddings learn and encode diverse contextual information associated with different types of layout annotation. Moreover, they play a vital role in providing the dataset’s global context information when queried by the compressed image feature F_c via cross-attention in our shared feature guidance module (refer to Sec. 4.3). By infusing our compressed feature F_c with this rich layout type-related embedding E_k , we generate diverse and meaningful predictions (P_{extended} and P_{enclosed}), each aligned with a distinct global context of the dataset label.

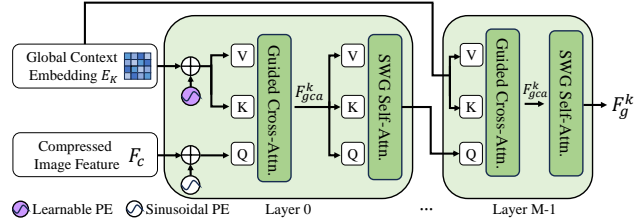


Figure 4. **Our Shared Feature Guidance Module architecture (SFGM)**. It consists of two blocks: Guided Cross-Attention and SWG Self-Attention. The module has $M = 8$ layers, and the structure of each layer is identical. Given the compressed image feature F_c and global context embedding E_k , we first apply the sinusoidal and learnable positional encoding, respectively. With the compressed feature F_c as the query Q and our global context embedding E_k as both the key K and value V , our guided cross-attention generates the feature F_{gca}^k , and it is served as QKV inputs to SWG self-attention. This process will repeat and further refine the output feature with our global context embedding to generate the final guided feature F_g^k .

4.3. Shared Feature Guidance Module

Building upon the compressed image feature F_c and the global context embeddings E_k , as shown in Fig. 3(c), we present an innovative component called *Shared Feature Guidance Module* (SFGM). This module can effectively guide the fusion of the image feature with the target global context embedding. Specifically, we share the compressed image feature F_c and use different global context embeddings E_k (one at a time) as the inputs for our shared feature guidance module $SFGM(\cdot)$ to generate corresponding guided feature $F_g^k \in \mathbb{R}^{N \times D}$, denoted as:

$$F_g^k = SFGM(F_c, E_k), k \in [\textit{extended}, \textit{enclosed}]. \quad (1)$$

Our shared feature guidance module consists of *Guided Cross-Attention* and *SWG Self-Attention* as the building blocks, and the details of the architecture are shown in Fig. 4.

The standard cross-attention setting in DETR [2] or other high-level tasks [4, 5, 20, 30, 37, 42] uses embeddings as the query Q to retrieve relevant information from the corresponding image feature, which acts as both the key K and value V in order to generate the target outputs. In our scenario, if we adopt the standard QKV setting, the shared image feature F_c alone may not carry sufficient information to distinguish between the two types of distinct layouts. Therefore, we reverse this relationship and use our global context embeddings E_k to learn from corresponding labels, guiding the image feature F_c to generate the desired layout types.

As shown in Fig. 4, we use the compressed feature F_c as the query Q and our global context embedding E_k as both the key K and value V in our guided cross-attention

$GCA(\cdot)$:

$$\begin{aligned} \mathbf{Q} &= (F_c + PE_{\sin})\mathbf{W}_q, & \mathbf{K} &= (E_k + PE_{\text{learn}})\mathbf{W}_k, \\ \mathbf{V} &= (E_k + PE_{\text{learn}})\mathbf{W}_v, & F_{gca}^k &= GCA(\mathbf{Q}, \mathbf{K}, \mathbf{V}), \end{aligned} \quad (2)$$

where $F_{gca}^k \in \mathbb{R}^{N \times D}$ is the output of our guided cross-attention block. We apply different positional encoding strategies for these features, utilizing learnable positional encoding [2] $PE_{\text{learn}} \in \mathbb{R}^{N \times D}$ for our global context embedding E_k and sinusoidal positional encoding [1, 21] $PE_{\sin} \in \mathbb{R}^{N \times D}$ for the compressed image feature F_c . Each feature is then multiplied by its respective learnable weights $\mathbf{W}_{q/k/v} \in \mathbb{R}^{D \times D}$. This unique design choice enables us to enrich the image feature F_c by effectively incorporating our global context embedding E_k . Subsequently, this enriched feature F_{gca}^k is served as \mathbf{QKV} inputs to the SWG self-attention module [17] for further enhancement. As demonstrated in [17], the SWG self-attention module can effectively establish local and global geometric relationships within the room layout. Then, the process of guided cross-attention and SWG self-attention is repeated several times to refine the image feature with our context embeddings to generate the final guided feature F_g^k , as shown in Fig. 4.

By employing this novel cross-attention design, we achieve an enriched and context-aware guided feature representation F_g^k that is subsequently utilized for generating our Bi-Layout predictions (P_{extended} and P_{enclosed}), each possessing distinct and valuable properties. This flexibility in our method enables us to provide diverse layout predictions tailored to different global context embeddings E_k and input panorama features F_c . Built on this architectural design, our model can be compact and efficient to generalize to more label types by increasing global context embeddings E_k .

4.4. Training Objective

After obtaining the target feature F_g^k , we follow [17, 29] using fully connected (FC) layers to map the feature F_g^k to horizon-depth $d_k = \{d_k^i\}_{i=1}^N$ and room height h_k , where N is the width of the feature map. We can apply the explicit transformation to convert the horizon depth and room height to layout boundaries P_k on the panorama. We further convert column-wise depth d_k^i into depth normal n_k^i and gradient of normal g_k^i , $k \in [\textit{extended}, \textit{enclosed}]$.

The loss functions for depth, normal, gradient, and room height are defined as follows:

$$\begin{aligned} \mathcal{L}_{\text{depth}}^k &= \frac{1}{N} \sum_{i \in N} |d_k^i - d_{\text{gt}}^i|, & \mathcal{L}_{\text{normal}}^k &= \frac{1}{N} \sum_{i \in N} (-n_k^i \cdot n_{\text{gt}}^i), \\ \mathcal{L}_{\text{gradient}}^k &= \frac{1}{N} \sum_{i \in N} |g_k^i - g_{\text{gt}}^i|, & \mathcal{L}_{\text{height}}^k &= |h_k - h_{\text{gt}}|, \end{aligned} \quad (3)$$

where d_{gt}^i , n_{gt}^i , g_{gt}^i , and h_{gt} denote the ground truth of depth, normal, gradient, and room height respectively. We calculate

the L1 loss for depth loss, gradient loss, height loss, and cosine similarity for normal loss. Our branch loss \mathcal{L}_k is:

$$\mathcal{L}_k = \lambda_d \mathcal{L}_{\text{depth}}^k + \lambda_n \mathcal{L}_{\text{normal}}^k + \lambda_g \mathcal{L}_{\text{gradient}}^k + \lambda_h \mathcal{L}_{\text{height}}^k, \quad (4)$$

where $k \in [\textit{extended}, \textit{enclosed}]$ and the final loss $\mathcal{L}_{\text{total}} = \mathcal{L}_{\text{extended}} + \mathcal{L}_{\text{enclosed}}$. We set $\lambda_d = 0.9$, $\lambda_n = 0.1$, $\lambda_g = 0.1$ and $\lambda_h = 0.1$ for both branches to balance the model weight.

5. Experiments

We conduct our experiments on a single NVIDIA RTX 4090 GPU and implement the proposed method with PyTorch [22]. For training, we use a batch size of 12 and set the learning rate to 1×10^{-4} . We select Adam as our optimizer, adhering to its default configurations. For the data augmentation, we use the technique proposed in [31], including left-right flipping, panoramic horizontal rotation, luminance adjustment, and panoramic stretch.

5.1. Datasets

MatterportLayout. MatterportLayout [45] contains 2295 samples labeled by Zou *et al.* [45]. However, as we analyzed in Sec. 3, this dataset has annotation ambiguity, and many images with ambiguity are annotated with the *extended* type. Hence, we propose a semi-automatic procedure (provide the details in supplementary material) to re-annotate *enclosed* type labels from the ambiguous *extended* ones. We re-annotate 15% of the labels in the whole dataset. Note that these new labels of *enclosed* type plus the remaining 85% of original labels will be used to train our Bi-Layout model’s *enclosed* branch. In contrast, all original labels will be used to train the *extended* branch. For a fair comparison with SoTA methods, we use the original label and the same testing split for evaluation.

ZInD. ZInD [7] dataset is currently the largest dataset with room layout annotations. It provides both *raw* and *visible* labels, which is similar to our defined *enclosed* and *extended* types, respectively. Besides, ZInD separates the data into *simple* and *complex* subsets based on whether the images have contiguous occluded corners. Therefore, we have two variants of ZInD in our experiments: **(a) ZInD-Simple** represents the *simple* subset and consists of 24882, 3080, and 3170 panoramas for training, validation, and testing splits. **(b) ZInD-All** represents the whole dataset with 50916, 6352, and 6352 panoramas for each split. It has complex opening regions, resulting in more severe ambiguity issues. Therefore, it can better evaluate the robustness of different methods for handling the ambiguity issue. In both ZInD dataset variants, we use the *raw* and *visible* labels to train our *enclosed* and *extended* branches, respectively, and follow the SoTA methods to test on *raw* labels for a fair comparison.

(a) Full set		MatterportLayout [45]		ZInD-Simple [7]		ZInD-All [7]	
Method	# Params	2DIoU(%)	3DIoU(%)	2DIoU(%)	3DIoU(%)	2DIoU(%)	3DIoU(%)
LED ² Net [34]	82 M	82.37	80.05	90.20	88.34	82.31	80.28
LGT-Net [17]	136 M	83.52	81.11	91.77	89.95	84.07	82.09
DOP-Net [29]	137 M	84.11	81.70	91.94	90.13	83.92	81.87
Ours (equivalent branch)	102 M	84.56	82.05	92.07	90.25	84.90	82.96
Ours (disambiguate)	102 M	85.10	82.57	92.79	90.95	86.21	84.22
(b) Subset		MatterportLayout [45]		ZInD-Simple [7]		ZInD-All [7]	
Method	# Params	2DIoU(%)	3DIoU(%)	2DIoU(%)	3DIoU(%)	2DIoU(%)	3DIoU(%)
LED ² Net [34]	82 M	53.57	51.12	45.31	44.10	48.76	47.35
LGT-Net [17]	136 M	53.17	50.54	53.20	52.00	50.89	49.58
DOP-Net [29]	137 M	57.13	54.80	51.55	50.26	50.92	49.46
Ours (equivalent branch)	102 M	59.85	57.08	55.09	53.76	54.22	52.78
Ours (disambiguate)	102 M	62.81	59.97	62.10	60.63	60.20	58.53

Table 1. **Full set and Subset evaluation.** **Equivalent branch** represents the output, which is trained with the same label as baseline methods. **Disambiguate** is our proposed metric.

5.2. Disambiguate Metric

If we already know the layout type of each test image, we can use this information to select the output from the corresponding branch for evaluation. However, we find that the test data has annotation ambiguity; even the *raw* labels in ZInD are still not exempt from this issue.

To address the above issue and demonstrate our model’s capability to handle the annotation ambiguity, we introduce a new metric, termed the *disambiguate* metric, as follows:

$$IoU_{\text{disambiguate}} = \sum_{i=0}^S \arg \max_{P_k^i \in \mathbb{P}} IoU(P_{\text{gt}}^i, P_k^i), \quad (5)$$

where $P_k^i \in \mathbb{P}$, $k \in [\textit{extended}, \textit{enclosed}]$ denotes layout predictions from both branches and P_{gt}^i denotes the ground truth layout. We first calculate the Intersection over Union (IoU) between each prediction and ground truth (GT) for each image and then select the higher IoU for averaging all samples. This is because the higher IoU serves as the disambiguate prediction and represents the most suitable prediction when encountering ambiguity.

The proposed metric effectively provides a robust and quantitative measure of how a method excels in handling ambiguous scenarios within the dataset without necessitating manual corrections to the ambiguous annotations. In other words, we can use the labels provided by the original dataset to do the evaluation.

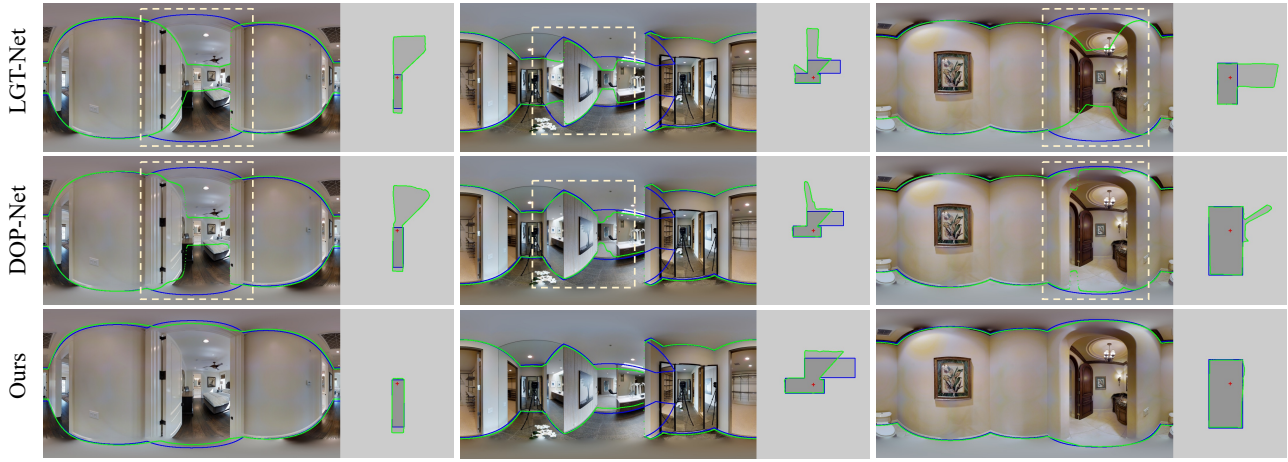
5.3. Comparison with State-of-the-Art Methods

Evaluation settings. Since our model outputs two layouts, we propose to compare our method with the SoTA methods in two ways. **Using the equivalent branch:** We use the output from the branch trained with the same data as other methods. Specifically, we use the output from *extended*

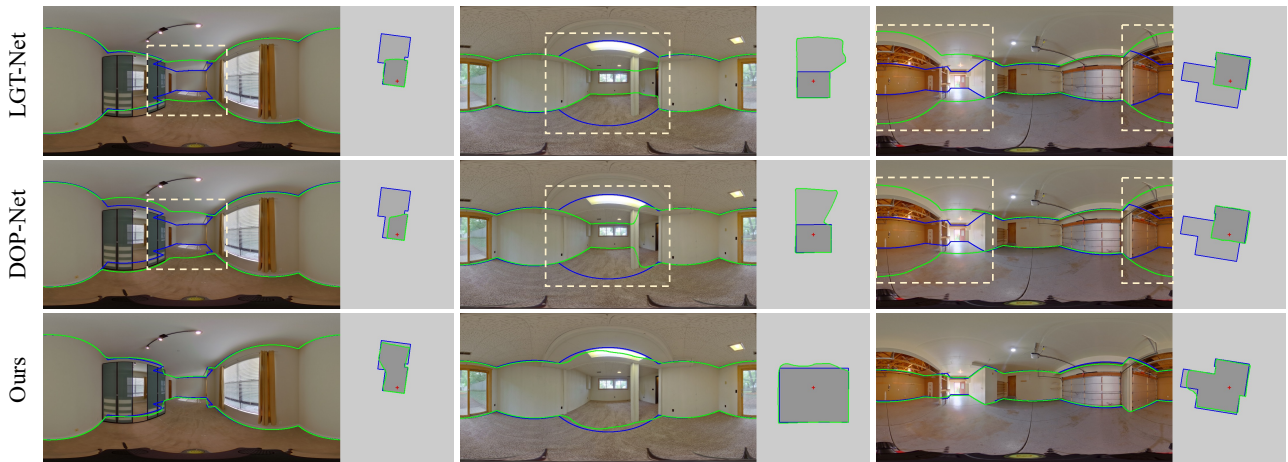
branch for the MatterportLayout dataset and the output from *enclosed* branch for ZInD to fairly compare with other methods. **Using both branches with disambiguate metric:** We use the proposed *disambiguate* metric as defined in Sec. 5.2 to evaluate the performance of our method.

Full set evaluation. We present quantitative results on three different datasets in Table 1(a). As the SoTA methods do not experiment on the ZInD-All dataset, we retrain all baseline models based on their official repositories. The results demonstrate that our *equivalent* branch consistently outperforms SoTA methods across all datasets, underscoring the advantages of joint training with bi-layout data. Furthermore, our disambiguated results surpass these benchmarks, affirming the existence of ambiguity in the original annotations. Our Bi-Layout model effectively mitigates this issue by selecting the most appropriate prediction. Notably, in terms of model size, our architecture, despite generating bi-layout predictions, maintains a smaller total parameter size compared to the SoTA models. This underscores the efficiency of our design in achieving superior performance with a more compact model.

Subset evaluation. To highlight the ambiguity issue, we select a subset based on the failure predictions of all the previous SoTA models [17, 29, 34]. For each SoTA model, we find images with the 2DIoU evaluation lower than 0.6. Next, we combine all these failure cases among all the SoTA models to construct the subset. Finally, the subsets consist of 11%, 6%, and 18% of the test data in three datasets, respectively. The quantitative results in Table 1(b) reveal a more pronounced performance gap between our method and the SoTA models, with differences reaching up to 9.28% in 2DIoU on the most ambiguous ZInD-All dataset. We also provide the qualitative results in Fig. 5, where a bird’s-



(a) Qualitative comparison on the MatterportLayout [45] dataset.



(b) Qualitative comparison on the ZInd [7] dataset.

Figure 5. **Qualitative comparison** on the MatterportLayout [45] (top) and ZInd [7] datasets (bottom). **Blue** and **Green** represent ground truth labels and predictions, respectively. The boundaries of the room layout are on the left, and their bird’s eye view projections are on the right. We show our *disambiguate* results, which effectively address the ambiguity issue, while the SoTA methods struggle with the ambiguity, as highlighted in dashed lines.

eye view of the predictions vividly illustrates the significant challenges posed by ambiguity. This confirms that layout ambiguity is a key cause for low IoUs of previous methods, and our Bi-Layout estimation is effective in addressing the issue and performs remarkably well in this subset.

5.4. Ambiguity Detection

Our Bi-Layout model can naturally detect ambiguous regions by comparing the per-column pixel difference between two predicted layout boundaries. This per-column pixel difference can serve as our predicted confidence score. If the difference is larger, the column is more likely to be an ambiguous region (i.e., typically an opening room structure). We formulate the detection of ambiguous regions into a binary classification task where GT ambiguous regions are columns with more than 2 pixels’ difference between two annotations of the *extended* and *enclosed* types. We predict



Figure 6. **Qualitative results for ambiguity detection.** **Blue** and **Green** on the top and bottom rows represent ground truth and predicted confidence, respectively. **Cyan** and **Magenta** lines are our *extended* and *enclosed* type layout predictions. With these two predictions, our model can accurately detect ambiguous regions.

columns with more than 10 pixels’ difference between predicted layouts as ambiguous regions. We test this method on ZInd as it is the only dataset that provides both types of GT

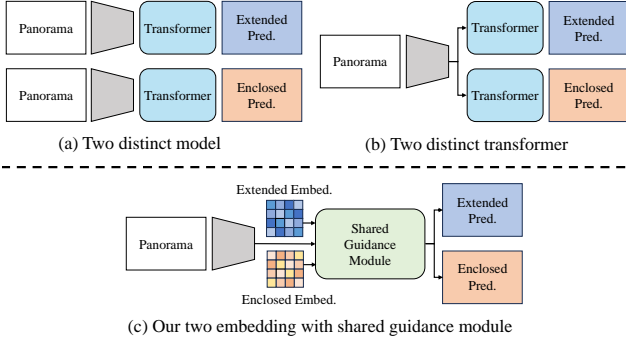


Figure 7. **Model architecture comparison.** We show the different model architecture designs for predicting multiple layouts. Please refer to Table 3 for quantitative comparison.

labels (*i.e.*, *raw* and *visible*) in testing. Our method achieves a reasonably high Precision of **0.82** and Recall of **0.71**. Moreover, the qualitative results in Fig. 6 further demonstrate that our method can indeed detect ambiguous regions. We believe this is particularly useful for applications where the model can highlight ambiguous regions and let the users select suitable predictions for their use cases.

5.5. Abalation Studies

Different feature fusion designs. To fuse the information from image features and our global context embeddings, we conduct comprehensive ablation studies to validate the effectiveness of different designs. The fusion methods include add, concatenation, AdaIn [16], and FiLM [23]. We further investigate two Query-Key-Value (QKV) feature designs in our shared feature guidance module.

The results in Table 2 show that our proposed design significantly outperforms all feature fusion methods and the standard cross-attention setting, where the global context embedding E_k served as query Q . The compressed image feature F_c served as key K and value V . This demonstrates that our design can effectively utilize contextual information within the embedding E_k to enhance the alignment of the compressed feature F_c with the corresponding layout prediction type.

Comparions of model architectures. As shown in Fig. 7, we compare three model architectures to predict multiple layouts. We conduct the quantitative comparison in Table 3. **Two models:** Training two models of the same architecture to predict two layout types is the most straightforward design (Fig. 7(a)). This architecture achieves good performance without interference between learning two types of layout. However, this doubles the model size and training time.

Two transformers: An alternative is to share the feature extractor but separate the transformer and prediction head (Fig. 7(b)). This saves model size a little, but the performance drops significantly as it cannot handle the interference when learning two types of layouts simultaneously.

Design	Q	KV	2D IoU (%)	3D IoU (%)
Add			83.79	81.26
Concat			84.17	81.44
AdaIn [16]			83.28	80.54
FiLM [23]			84.08	81.39
Standard	E_k	F_c	83.34	80.85
Ours	F_c	E_k	85.10	82.57

Table 2. **Comparison of QKV feature designs.** F_c is the compressed feature, and E_k is our global context embedding. We evaluate different designs of QKV features in the Shared Feature Guidance Module on MatterportLayout [45] with our proposed *disambiguate* metric.

Method	# Params	2DIoU(%)	3DIoU(%)
Two models	272 M	85.29	82.72
Two Transformers	203 M	84.35	81.88
Ours (c = 1024)	172 M	85.25	82.76
Ours (c = 512)	102 M	85.10	82.57

Table 3. **Model size and performance trade-off.** In this part, we only compare to the LGT-Net [17] model variances (*i.e.*, The first two rows) since our model is built on top of its architecture. In the third row, c represents the # channel of the image feature. We conduct these quantitative evaluations on MatterportLayout [45] with our proposed *disambiguate* metric. Our final model strikes the best balance between performance and parameter efficiency.

Our model: Our model is the smallest as we share both the feature extractor and transformer and only separate the lightweight prediction head (Fig. 7(c)). To reduce the interference in learning two layouts, we introduce two learnable global context embeddings, which can inject layout type-related context information into the image feature via cross-attention. Therefore, our model achieves comparable or better performance than others. In addition, there is only a slight performance drop if we further reduce the model size by reducing the compressed feature channel dimension from 1024 to 512. Our final model ($c = 512$) balances performance and parameter efficiency best.

6. Conclusion

We propose a novel Bi-Layout model to generate two distinct predictions, effectively resolving the layout ambiguity. Most importantly, we introduce a novel embedding mechanism with a shared feature guidance module, where each embedding is designed to learn the global context inherent in each type of layout. Our model strikes a good balance between model compactness and prediction accuracy with these designs. In addition, we propose a *disambiguate* metric to evaluate the accuracy with multiple predictions. On MatterportLayout [45] and ZInD [7] datasets, our method outperforms other state-of-the-art methods, especially on the subset setting with considerable ambiguity.

References

- [1] Irwan Bello, Barret Zoph, Ashish Vaswani, Jonathon Shlens, and Quoc V Le. Attention augmented convolutional networks. In *ICCV*, 2019. 5
- [2] Nicolas Carion, Francisco Massa, Gabriel Synnaeve, Nicolas Usunier, Alexander Kirillov, and Sergey Zagoruyko. End-to-end object detection with transformers. In *ECCV*, 2020. 2, 3, 4, 5
- [3] Xiaoxue Chen, Hao Zhao, Guyue Zhou, and Ya-Qin Zhang. Pq-transformer: Jointly parsing 3d objects and layouts from point clouds. *IEEE Robotics and Automation Letters*, 2022. 1
- [4] Bowen Cheng, Alex Schwing, and Alexander Kirillov. Per-pixel classification is not all you need for semantic segmentation. *NeurIPS*, 2021. 2, 3, 4
- [5] Bowen Cheng, Ishan Misra, Alexander G Schwing, Alexander Kirillov, and Rohit Girdhar. Masked-attention mask transformer for universal image segmentation. In *CVPR*, 2022. 2, 3, 4
- [6] James M Coughlan and Alan L Yuille. Manhattan world: Compass direction from a single image by bayesian inference. In *ICCV*, 1999. 3
- [7] Steve Cruz, Will Hutchcroft, Yuguang Li, Naji Khosravan, Ivaylo Boyadzhiev, and Sing Bing Kang. Zillow indoor dataset: Annotated floor plans with 360deg panoramas and 3d room layouts. In *CVPR*, 2021. 1, 5, 6, 7, 8, 11, 12, 13, 15, 16
- [8] Clara Fernandez-Labrador, Jose M Facil, Alejandro Perez-Yus, Cédric Demonceaux, Javier Civera, and Jose J Guerrero. Corners for layout: End-to-end layout recovery from 360 images. *IEEE Robotics and Automation Letters*, 2020. 3
- [9] Ned Greene. Environment mapping and other applications of world projections. *IEEE Computer Graphics and Applications*, 1986. 3
- [10] Abhinav Gupta, Martial Hebert, Takeo Kanade, and David Blei. Estimating spatial layout of rooms using volumetric reasoning about objects and surfaces. *NeurIPS*, 2010. 3
- [11] Kaiming He, Xiangyu Zhang, Shaoqing Ren, and Jian Sun. Deep residual learning for image recognition. In *CVPR*, 2016. 4
- [12] Varsha Hedau, Derek Hoiem, and David Forsyth. Recovering the spatial layout of cluttered rooms. In *ICCV*, 2009. 3
- [13] Martin Hirzer, Vincent Lepetit, and PETER ROTH. Smart hypothesis generation for efficient and robust room layout estimation. In *WACV*, 2020. 3
- [14] Sepp Hochreiter and Jürgen Schmidhuber. Long short-term memory. *Neural Computation*, 1997. 3
- [15] Siyuan Huang, Siyuan Qi, Yixin Zhu, Yinxue Xiao, Yuanlu Xu, and Song-Chun Zhu. Holistic 3d scene parsing and reconstruction from a single rgb image. In *ECCV*, 2018. 1
- [16] Xun Huang and Serge Belongie. Arbitrary style transfer in real-time with adaptive instance normalization. In *ICCV*, 2017. 8
- [17] Zhigang Jiang, Zhongzheng Xiang, Jinhua Xu, and Ming Zhao. Lgt-net: Indoor panoramic room layout estimation with geometry-aware transformer network. In *CVPR*, 2022. 1, 3, 4, 5, 6, 8, 14
- [18] Thomas N Kipf and Max Welling. Semi-supervised classification with graph convolutional networks. In *ICLR*, 2017. 3
- [19] Arun Mallya and Svetlana Lazebnik. Learning informative edge maps for indoor scene layout prediction. In *ICCV*, 2015. 3
- [20] Tim Meinhardt, Alexander Kirillov, Laura Leal-Taixe, and Christoph Feichtenhofer. Trackformer: Multi-object tracking with transformers. In *CVPR*, 2022. 2, 3, 4
- [21] Niki Parmar, Ashish Vaswani, Jakob Uszkoreit, Lukasz Kaiser, Noam Shazeer, Alexander Ku, and Dustin Tran. Image transformer. In *ICML*, 2018. 5
- [22] Adam Paszke, Sam Gross, Francisco Massa, Adam Lerer, James Bradbury, Gregory Chanan, Trevor Killeen, Zeming Lin, Natalia Gimelshein, Luca Antiga, et al. Pytorch: An imperative style, high-performance deep learning library. *NeurIPS*, 2019. 5
- [23] Ethan Perez, Florian Strub, Harm De Vries, Vincent Dumoulin, and Aaron Courville. Film: Visual reasoning with a general conditioning layer. In *AAAI*, 2018. 8
- [24] Giovanni Pintore, Marco Agus, and Enrico Gobbetti. Atlantanet: inferring the 3d indoor layout from a single 360° image beyond the manhattan world assumption. In *ECCV*, 2020. 3
- [25] Srikumar Ramalingam, Jaishanker K Pillai, Arpit Jain, and Yuichi Taguchi. Manhattan junction catalogue for spatial reasoning of indoor scenes. In *CVPR*, 2013. 3
- [26] Yuzhuo Ren, Shangwen Li, Chen Chen, and C-C Jay Kuo. A coarse-to-fine indoor layout estimation (cfile) method. In *ACCV*, 2017. 3
- [27] Mike Schuster and Kuldip K Paliwal. Bidirectional recurrent neural networks. *IEEE Transactions on Signal Processing*, 1997. 3
- [28] Alexander G Schwing and Raquel Urtasun. Efficient exact inference for 3d indoor scene understanding. In *ECCV*, 2012. 3
- [29] Zhijie Shen, Zishuo Zheng, Chunyu Lin, Lang Nie, Kang Liao, Shuai Zheng, and Yao Zhao. Disentangling orthogonal planes for indoor panoramic room layout estimation with cross-scale distortion awareness. In *CVPR*, 2023. 1, 3, 4, 5, 6
- [30] Jheng-Wei Su, Kuei-Yu Tung, Chi-Han Peng, Peter Wonka, and Hung-Kuo Chu. Slibo-net: Floorplan reconstruction via slicing box representation with local geometry regularization. In *NeurIPS*, 2023. 2, 3, 4
- [31] Cheng Sun, Chi-Wei Hsiao, Min Sun, and Hwann-Tzong Chen. Horizonnet: Learning room layout with 1d representation and pano stretch data augmentation. In *CVPR*, 2019. 1, 3, 4, 5
- [32] Cheng Sun, Min Sun, and Hwann-Tzong Chen. Hohonet: 360 indoor holistic understanding with latent horizontal features. In *CVPR*, 2021. 1, 3
- [33] Ashish Vaswani, Noam Shazeer, Niki Parmar, Jakob Uszkoreit, Llion Jones, Aidan N Gomez, Łukasz Kaiser, and Illia Polosukhin. Attention is all you need. *NeurIPS*, 2017. 3
- [34] Fu-En Wang, Yu-Hsuan Yeh, Min Sun, Wei-Chen Chiu, and Yi-Hsuan Tsai. Led2-net: Monocular 360deg layout estimation via differentiable depth rendering. In *CVPR*, 2021. 1, 3, 4, 6

- [35] Huayan Wang, Stephen Gould, and Daphne Roller. Discriminative learning with latent variables for cluttered indoor scene understanding. *Communications of the ACM*, 2013. [3](#)
- [36] Shang-Ta Yang, Fu-En Wang, Chi-Han Peng, Peter Wonka, Min Sun, and Hung-Kuo Chu. Dula-net: A dual-projection network for estimating room layouts from a single rgb panorama. In *CVPR*, 2019. [3](#)
- [37] Yuanwen Yue, Theodora Kontogianni, Konrad Schindler, and Francis Engelmann. Connecting the dots: Floorplan reconstruction using two-level queries. In *CVPR*, 2023. [2](#), [3](#), [4](#)
- [38] Cheng Zhang, Zhaopeng Cui, Yinda Zhang, Bing Zeng, Marc Pollefeys, and Shuaicheng Liu. Holistic 3d scene understanding from a single image with implicit representation. In *CVPR*, 2021. [1](#)
- [39] Hao Zhao, Ming Lu, Anbang Yao, Yiwen Guo, Yurong Chen, and Li Zhang. Physics inspired optimization on semantic transfer features: An alternative method for room layout estimation. In *CVPR*, 2017. [3](#)
- [40] Kai Zhao, Qi Han, Chang-Bin Zhang, Jun Xu, and Ming-Ming Cheng. Deep hough transform for semantic line detection. *TPAMI*, 2021. [3](#)
- [41] Yining Zhao, Chao Wen, Zhou Xue, and Yue Gao. 3d room layout estimation from a cubemap of panorama image via deep manhattan hough transform. In *ECCV*, 2022. [3](#)
- [42] Xingyi Zhou, Tianwei Yin, Vladlen Koltun, and Philipp Krähenbühl. Global tracking transformers. In *CVPR*, 2022. [2](#), [3](#), [4](#)
- [43] Xizhou Zhu, Weijie Su, Lewei Lu, Bin Li, Xiaogang Wang, and Jifeng Dai. Deformable detr: Deformable transformers for end-to-end object detection. In *ICLR*, 2021. [3](#)
- [44] Chuhan Zou, Alex Colburn, Qi Shan, and Derek Hoiem. Layoutnet: Reconstructing the 3d room layout from a single rgb image. In *CVPR*, 2018. [3](#)
- [45] Chuhan Zou, Jheng-Wei Su, Chi-Han Peng, Alex Colburn, Qi Shan, Peter Wonka, Hung-Kuo Chu, and Derek Hoiem. Manhattan room layout reconstruction from a single 360° image: A comparative study of state-of-the-art methods. *IJCV*, 2021. [1](#), [2](#), [3](#), [5](#), [6](#), [7](#), [8](#), [11](#), [12](#), [13](#), [14](#), [15](#), [16](#)

No More Ambiguity in 360° Room Layout via Bi-Layout Estimation

Supplementary Material

A. Overview

This supplementary material presents additional results to complement the main manuscript. We first introduce our relabeling pipeline in Sec. B and show some bi-layout annotation examples in Sec. C. In Sec. D, we provide more qualitative comparisons with the state-of-the-art (SoTA) methods. In Sec. E, we show more examples of our ambiguity detection under different scenarios to validate the robustness of our method. We conduct additional ablation studies in Sec. F to compare our method in more comprehensive settings. Finally, we show the limitations in Sec. G and provide some future research directions in Sec. H.

B. Semi-automatic Relabeling

We introduce our semi-automatic relabeling pipeline for annotating the second type of layout on the MatterportLayout [45] dataset as follows and shown in Fig. 8:

- (a) Given the original annotations from the MatterportLayout [45] dataset. We check each column of the panorama, if there are more than two annotations in the same column, we define it as the occlusion part. As shown in Fig. 8(a), **blue line** indicates the original annotation, and the dashed lines highlight the occlusion region in the original region.
- (b) Next, we take the original annotation and project it to the bird's-eye view floorplan coordinate, aligning it with the center of the camera. As shown in Fig. 8(b), the isolated **red point** indicates the center of the camera.
- (c) After obtaining the annotation on the floorplan coordinate, we categorize the corners as either *visible* or *invisible*, representing whether the corners can be seen from the center of the camera or not. We find the closest *visible* points in the occlusion region as our candidate corners. As shown in Fig. 8(c), the **red boxes** indicate our candidate visible corners.
- (d) Once we have our candidate corners, we generate several annotation proposals using these points. As shown in Fig. 8(d), the **red lines** are our annotation proposals based on the candidate corners.
- (e) We select the best proposal, which should provide a clear boundary between different rooms. Note that this is the only step that needs a human decision. As shown in Fig. 8(e), we manually choose the proposal to separate the two rooms in this case.
- (f) Finally, we project these newly defined corners back to the panorama view, creating our relabeled annotation for the panorama. As shown in Fig. 8(f), **green line** indicates the relabeled annotation.

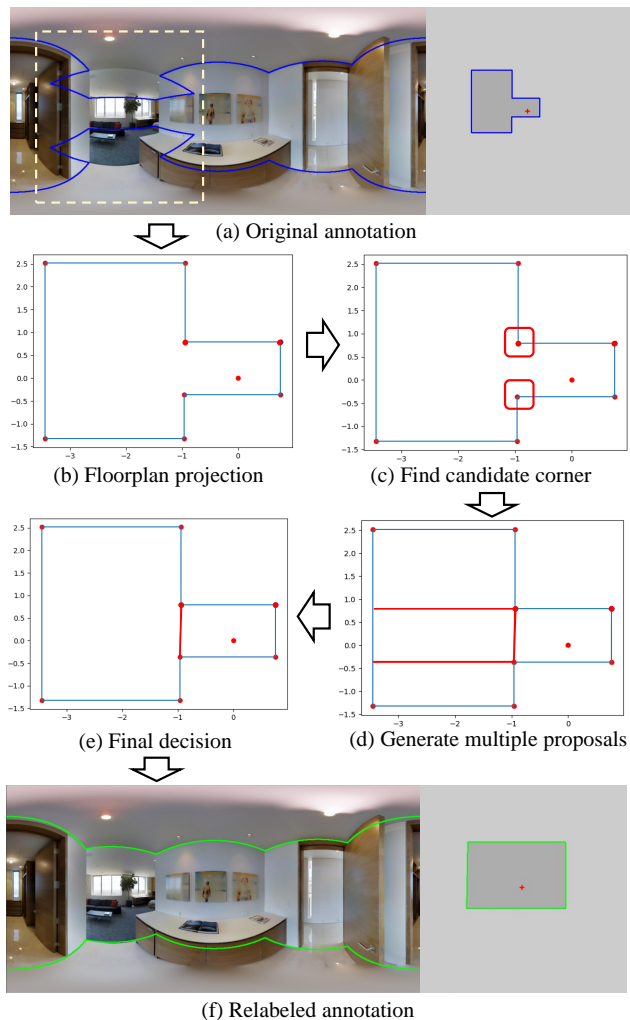


Figure 8. **Our relabeling pipeline.** **Blue line** in (a) and **Green line** in (f) represent the **original annotation** and **our relabeled annotation**, respectively. The layout boundaries are shown on the left, and their bird's-eye view projections are on the right. The dashed lines in (a) highlight the occlusion region in the original label.

We introduce our semi-automatic relabeling pipeline with the above steps, which clearly explain how we relabel the MatterportLayout [45] dataset. With this relabel pipeline, we can generate the *enclosed* type of annotations from the *extended* type of annotations and use these new labels with the original labels to train our Bi-Layout model.

C. Bi-layout Annotations

We show some bi-layout annotation examples in both the MatterportLayout [45] and ZInD [7] dataset.

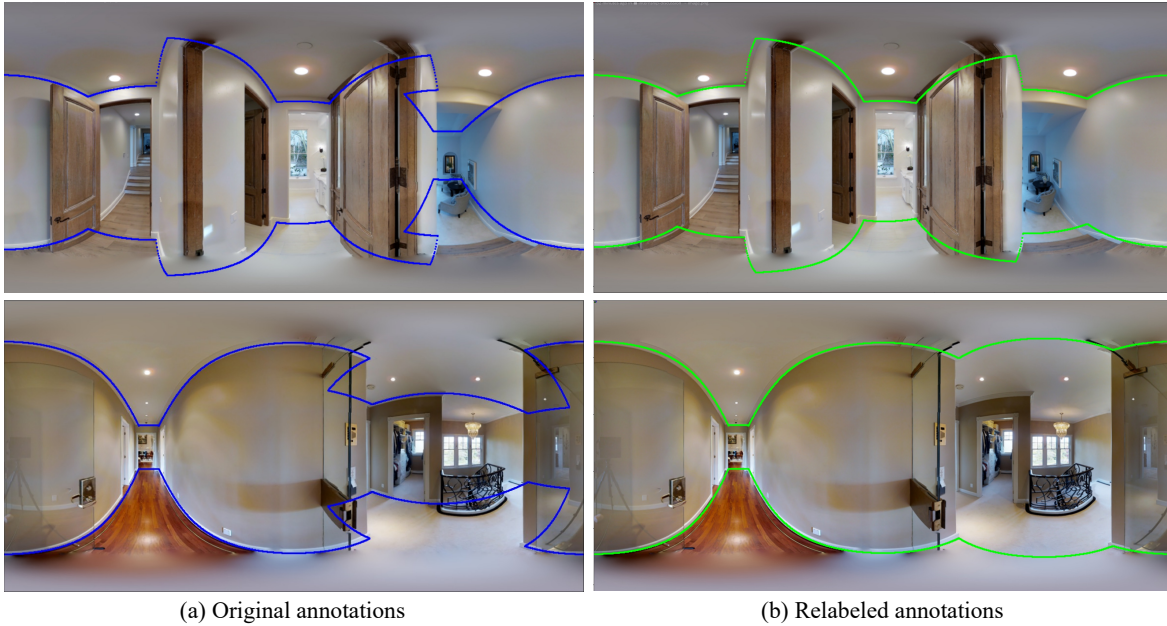


Figure 9. **Bi-layout annotations on the MatterportLayout [45] dataset.** Blue and Green lines indicate original and reabeled annotations.

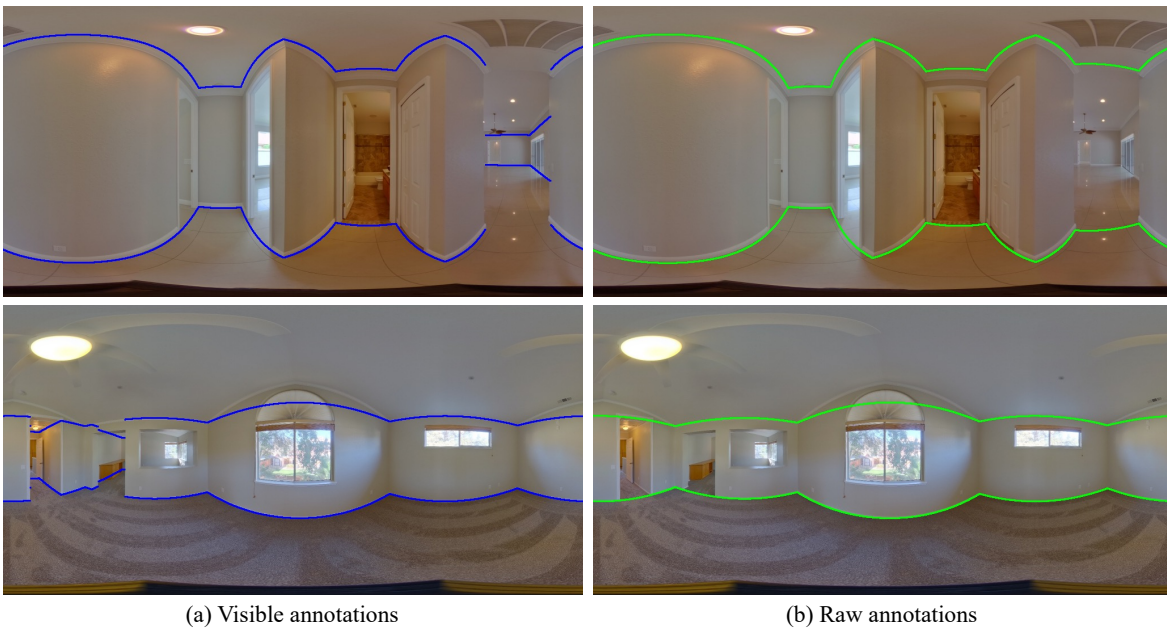


Figure 10. **Bi-layout annotations on the ZInD [7] dataset.** Blue and Green lines indicate *visible* and *raw* annotations.

MatterportLayout We present some cases of our reabeled annotations for the MatterportLayout [45] dataset. The original annotations in Fig. 9(a) are from the original dataset labels. Our reabeled annotations are shown in Fig. 9(b). Based on our definition, we relabel the *extended* type of annotation to the *enclosed* type of annotation.

ZInD We show some cases of two types of annotations officially provided by ZInD [7] dataset. The *visible* annotations are shown in Fig. 10(a), and the *raw* annotations are shown in Fig. 10(b), which corresponds to our *extended* type and *enclosed* type, respectively.

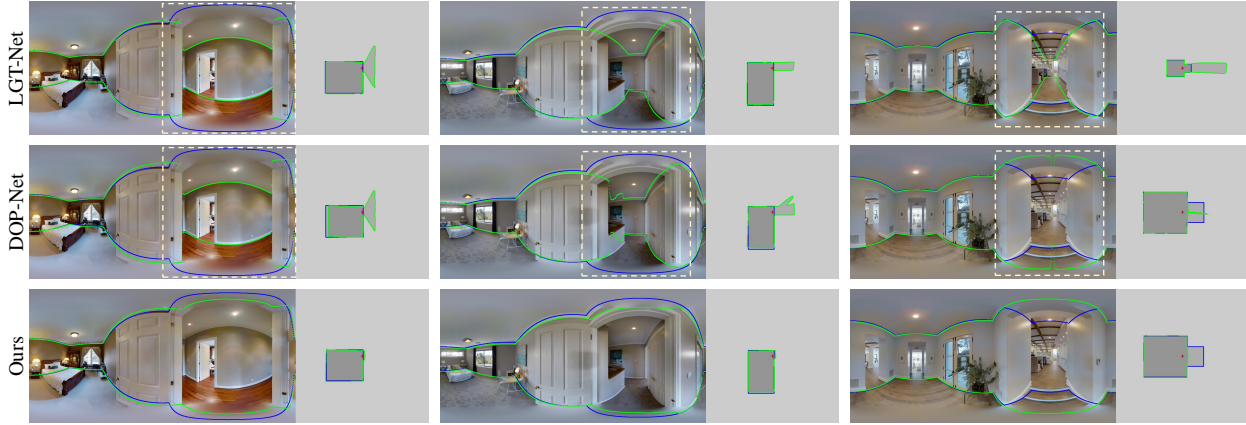


Figure 11. **More qualitative results on the MatterportLayout [45] dataset.** Blue and Green represent ground truth labels and predictions, respectively. The boundaries of the room layout are on the left, and their bird’s-eye view projections are on the right. We show our *disambiguate* results, which effectively address the ambiguity issue, while the SoTA methods struggle with the ambiguity, as highlighted in dashed lines.

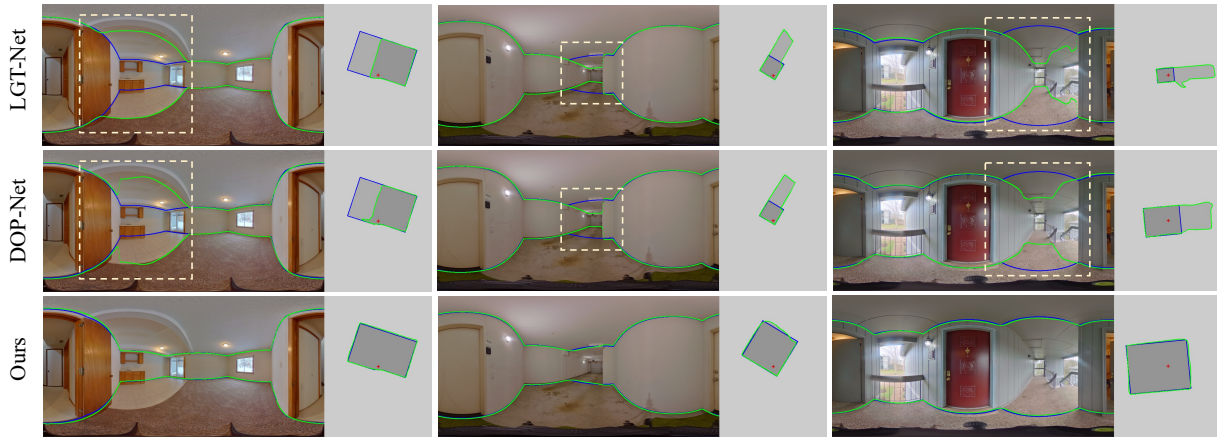


Figure 12. **More qualitative results on the ZInD [7] dataset.** Blue and Green represent ground truth labels and predictions, respectively. The boundaries of the room layout are on the left, and their bird’s-eye view projections are on the right. We show our *disambiguate* results, which effectively address the ambiguity issue, while the SoTA methods struggle with the ambiguity, as highlighted in dashed lines.

D. Comparisons with SoTA

We show more qualitative results on the MatterportLayout [45] dataset in Fig. 11 and the ZInD [7] dataset in Fig. 12. Our Bi-Layout model can effectively address the ambiguity issue that the SoTA methods struggle with.

E. Ambiguity Detection

We show more qualitative results and several scenarios of ambiguity detection in Fig. 13. In (a) and (b), we provide more examples to demonstrate that our Bi-Layout model can accurately detect ambiguous regions as the GT shows. In (c), we offer a normal case where there is no ambiguous region in the image, and our model can predict two identical predic-

tions. In (d), we show a special case where the GT does not indicate the ambiguous regions as it should be (i.e., GT itself has ambiguity), and our model can still successfully identify them, showing the capability of our method to address the inherent ambiguity issue in the dataset.

F. Ablation Studies

Global Context Embedding. To show the effectiveness of our proposed *Global Context Embedding* and *Shared Feature Guidance Module*, we conduct the experiment using a *single* global context embedding for our feature guidance module and only generate a *single* prediction as the conventional methods present (i.e., a single branch version of our proposed method). We compare our single branch with LGT-

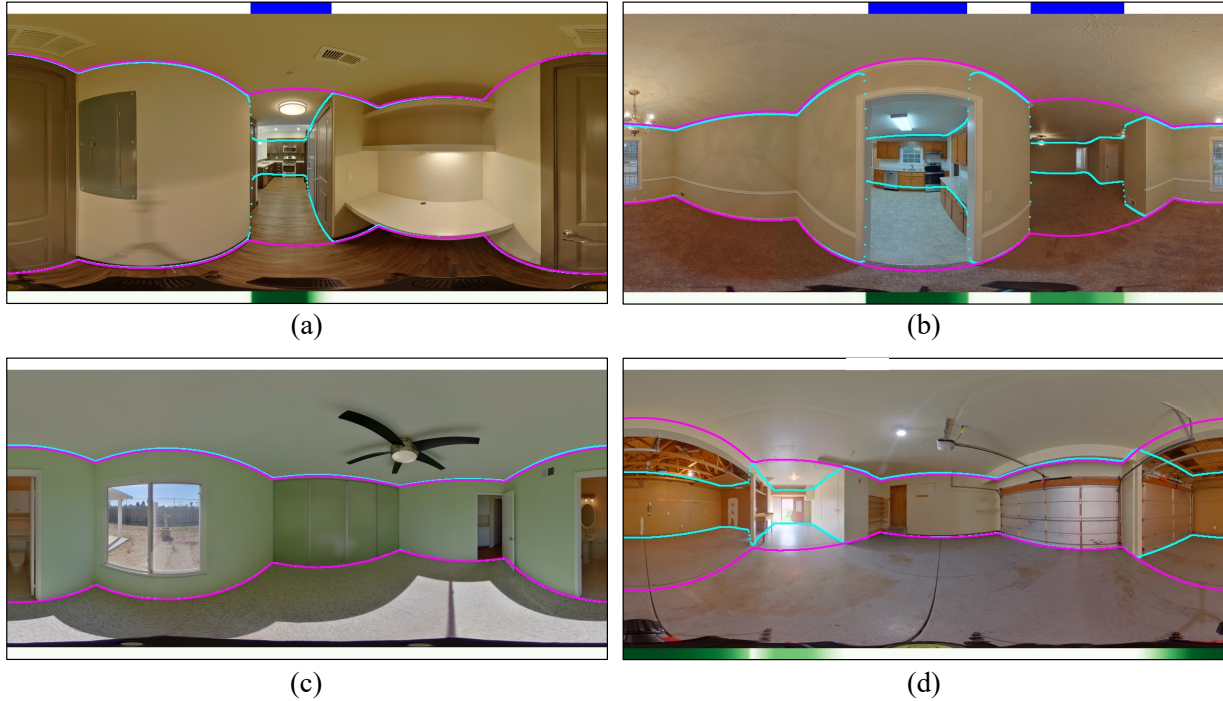


Figure 13. **Qualitative results and different scenarios for ambiguity detection.** Blue and Green on the top and bottom rows per image represent ground truth and predicted confidence, respectively. Cyan and Magenta lines are our *extended* and *enclosed* type layout predictions. In (a) and (b), our Bi-Layout model can accurately detect ambiguous regions as the GT shows. In (c), our model is able to predict two identical predictions when there is no ambiguous region in the image. In (d), we show a special case where the GT does not indicate the ambiguous regions as it should be (i.e., GT itself has ambiguity), and our model can still successfully identify them. Note that (d) is the example we show in the main manuscript where the SoTA methods fail, which corroborates the ambiguity in this image.

Method	# Params	Full set		Subset	
		2DIoU(%)	3DIoU(%)	2DIoU(%)	3DIoU(%)
LGT-Net [17]	136 M	83.52	81.11	53.17	50.54
Our single branch	102 M	84.09	81.78	58.65	56.23

Table 4. **Global Context Embedding for a single branch.** We conduct the experiment on both the full set and subset of the MatterportLayout [45] dataset. We choose LGT-Net [17] as our baseline method to compare the effectiveness of our Global Context Embedding design.

Net [17] since the proposed components are built on top of its architecture. In Table 4, our single branch outperforms the baseline method on both the full set and subset of the MatterportLayout [45] dataset, showing the effectiveness of our Global Context Embedding design.

Model size comparison. As discussed in the main manuscript, many model variations can let the SoTA method predict two layouts. We additionally show the *two-head* version of the baseline model, which shares the feature extractor and transformer parts, and simply add the other prediction head to generate the second type of layout. We compare all the model variations in Table 5. Although the *two-head* version model decreases the model parameters, the performance

is degraded significantly due to the naive model design. The comparison with these model variations shows the effectiveness and compactness of our Bi-Layout model.

Image feature dimension. To make the model more compact, we compare different image feature dimensions: 1024, 512, and 256. We experiment on the full set and subset of the MatterportLayout [45] dataset. In Table 6, the feature dimension of 1024 performs the best but it has the largest model size. Our proposed Bi-Layout model with a feature dimension of 512 strikes a good balance between the performance and model size. When it comes to the feature dimension of 256, the performance significantly drops, which means too small feature dimensions are not feasible for our task.

Method	# Params	Full set		Subset	
		2DIoU(%)	3DIoU(%)	2DIoU(%)	3DIoU(%)
Two models	272 M	85.29	82.72	62.54	60.04
Two transformers	203 M	84.35	81.88	59.21	56.80
Two heads	136 M	84.06	81.51	57.97	55.47
Ours (c = 512)	102 M	85.10	82.57	62.81	59.97

Table 5. **Model size and performance trade-off.** We conduct the experiment on both the full set and subset of the MatterportLayout [45] dataset and evaluate with our proposed *disambiguate* metric.

Method	# Params	Full set		Subset	
		2DIoU(%)	3DIoU(%)	2DIoU(%)	3DIoU(%)
Ours (c = 1024)	172 M	85.25	82.76	63.33	60.50
Ours (c = 512)	102 M	85.10	82.57	62.81	59.97
Ours (c = 256)	80 M	84.47	81.90	60.39	57.83

Table 6. **Different image feature dimensions.** We conduct the experiment on the full set and subset of the MatterportLayout [45] dataset and evaluate with our proposed *disambiguate* metric.

Model	2D IoU (%)	3D IoU (%)
Train from scratch	85.10	82.57
Pretrain on ZInD-Simple	85.52	83.28
Pretrain on ZInD-All	85.81	83.52

Table 7. **Pretraining effectiveness** on MatterportLayout [45] with our proposed *disambiguate* metric. The pretraining on different types of ZInD [7] datasets indeed helps the model to disambiguate, and the more data for the pretraining stage, the more performance gain it has.

Pretrain with more data. MatterportLayout [45] has limited bi-layout samples, with only 15% of 1647 training images being re-annotated. However, most images in ZInD-Simple [7] (24,882) and ZInD-All [7] (50,916) have both *raw* and *visible* labels. Although ZInD also has ambiguity issues, we believe pretraining on ZInD with extensive and diverse bi-layouts can boost the model’s performance on MatterportLayout. Therefore, we train one model from scratch and fine-tune two models pre-trained on ZInD-Simple and ZInD-All, respectively. The results in Table 7 demonstrate that pretraining indeed aids the model in disambiguating, with a more significant performance gain observed when more data is used during the pretraining stage. This suggests that with additional bi-layout annotations, our model has the potential to more effectively address the ambiguity issue.

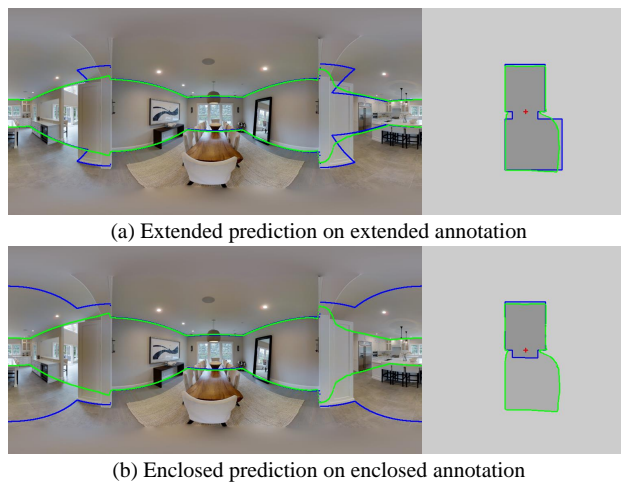


Figure 14. **Failure case on the MatterportLayout [45] dataset.** Blue and Green represent ground truth labels and predictions, respectively. The boundaries of the room layout are on the left, and their bird’s eye view projections are on the right.

G. Limitations

Our Bi-Layout model also has limitations. As shown in Fig. 14, we provide the predictions from our two branches, which aim to fit *extended* and *enclosed* annotations. We find that the main type of failure case comes from the large opening region, and there is no obvious room boundary to separate the different rooms. To address this difficult sce-

nario, we believe there is a need for more diverse bi-layout training data to ensure our model can learn the corresponding label properties.

H. Future Directions

We provide possible future research directions based on our current proposed method.

Cross-dataset training. Our main manuscript shows that pretraining on the large-scale ZInD [7] dataset can benefit the model performance evaluated on the MatterportLayout [45] dataset. This observation provides the possible direction for cross-dataset training, which may further improve the model performance.

Bi-Layout to multiple layouts. Our Bi-Layout model can generate two types of predictions. Based on our network design, it is possible to extend the number of predictions to more than two predictions. In the future, once the dataset provides multiple types of labels, multiple predictions can be achieved by simply adding more global context embeddings and the corresponding prediction heads. Most importantly, due to our shared feature guidance module design, those additional components for multiple predictions are very lightweight, which can still maintain the compactness of our model.